Check for updates

Numerical simulation of lead-free vacancy ordered Cs₂PtI₆ based perovskite solar cell using SCAPS-1D†

Akfeen Amjad,‡[a] Samina Qamar,‡[ab] Chengchen Zhao,[b] Kalsoom Fatima,[a] Muhammad Sultan [iD] *[c] and Zareen Akhter [iD] *[a]

In recent years, vacancy-ordered halide double perovskites have emerged as promising non-toxic and stable alternatives for their lead-based counterparts in optoelectronic applications. In particular, vacancy ordered Cs₂PtI₆ has emerged as a star material because of its high absorption coefficient, band gap of 1.37 eV, and long minority carrier lifetime. Despite substantial experimental research on this new class of material, theoretical simulations of their device properties remain scarce. In this work, a novel n-i-p device architecture (FTO/SnO₂/Cs₂PtI₆/MoO₃/C) is theoretically investigated using a solar cell capacitance simulator (SCAPS-1D). Theoretical investigations are carried out in order to optimize the device performance structure by varying the perovskite and selective charge transport layer thickness, absorber and interface defect density, operating temperature, back contact, series and shunt resistance, respectively. The optimized device showed an impressive power conversion efficiency (PCE) of 23.52% at 300 K, which is higher than the previously reported values. Subsequent analysis of the device's spectral response indicated that it possessed 98.9% quantum efficiency (QE) and was visibly active. These findings will provide theoretical guidelines for enhancing the performance of Cs₂PtI₆-based photovoltaic solar cells (PSCs) and pave the way for the widespread implementation of environmentally benign and stable perovskites.

1 Introduction

In recent years, there has been an increasing interest in hybrid perovskite solar cells (HPSCs) due to their remarkable intrinsic properties, including lower production costs, higher carrier mobilities, tunable band gaps, long carrier diffusion lengths, and high absorption coefficient.[1–4] In just over a decade, the PCE has dramatically increased from 3.3% to 25.7% due to the synergistic optimization of device interfaces. Full industrialization of HPSCs, in spite of having achieved a PCE of over 25% is trammeled by two main issues: Pb toxicity and instability. Organic ions methyl ammonium (MA⁺) and formamidinium (FA⁺) at the 'A' site of perovskite are unstable and degrade in atmospheric operational conditions.[5–10] Consequently, it would be highly advantageous for device lifetimes and environmental and health considerations regarding production and reprocessing to seek out non-toxic and stable perovskites that sustain

high efficiency. Materials such as (MA, Cs, Rb)₃Sb₂I₉, Cs₂PdBr₆, Cs₂AgBiBr₆, Cs₂AgBiI₆, Cs₂TiBr₆, AgBiI₄, CsGe₀.₅Sn₀.₅I₃, and Cs₂Au₂I₆ have been explored as lead-free alternatives, but their performance for photovoltaic applications has been disappointing.[11–21]

Finding stable, non-toxic, and highly efficient perovskites has proven to be an enormous problem to date. In recent years, A₂BX₆ (A═Cs; B═Te, Sn, Pt, Ti; X═I) double perovskites have garnered the attention of numerous researchers. These lead-free double perovskites demonstrate good stability and appropriate band gaps, making them viable candidates for future solar cell applications. As one of the most extensively studied vacancy-ordered halide double perovskites, Cs₂SnI₆ is a defect version of the three-dimensional (3D) CsSnI₃ perovskite with half of the Sn atoms in the Sn-centered octahedron absent. In the fabrication of solar cells, the inefficiency of Cs₂SnI₆ is a problem. Cs₂SnI₆-based solar cells have an efficiency of approximately 1.5%, while Cs₂SnI₄Br₂-based solar cells with mixed halides have an efficiency of 2.025%.

Cs₂PtI₆ is one of the intriguing materials in the A₂BX₆ class. Cs₂PtI₆ is an ideal option for PSCs due to its higher carrier mobility, higher absorption coefficient (4 × 10⁵ cm⁻¹), narrow band gap (1.37 eV), and dynamically stable structure.[22] With a tolerance factor of 0.97, it is able to have a highly consistent cubic structure, hence increasing its stability. It is stable under harsh conditions, including high temperatures, UV light, and

[a]Department of Chemistry, Quaid-i-Azam University (QAU), Islamabad 45320, Pakistan. E-mail: zareenakhter@yahoo.com; zareen_a@qau.edu.pk

[b]School of Chemistry, University of Glasgow, Glasgow, UK. E-mail: 2792248Z@student.gla.ac.uk

[c]Department of Physics, Kohsaar University Muree (KUM), Muree, Pakistan. E-mail: mssatti79@yahoo.com; Tel: (+92) 51-9269174

† Electronic supplementary information (ESI) available. See DOI: https://doi.org/10.1039/d3ra04176j

‡ Both these authors contributed equally.

high humidity.[23] It could serve as an appropriate substitute for perovskite-containing lead due to its oxidation resistance, high atomic number, and stability beyond non-toxicity. Cs_2PtI_6 is a highly advantageous photovoltaic material due to all of these qualities.

Unfortunately, systematic simulation and device modeling for the properties of Cs_2PtI_6 perovskite, which are essential for their optoelectronic devices, are rarely investigated, resulting in subpar device performance. To further improve the performance of Cs_2PtI_6-based PSCs, it is required to construct a band structure that minimizes charge recombination while enhancing carrier separation and transport. For this objective, device simulation is used to gain a comprehensive understanding of the relationship between the properties of materials and performance parameters. Using SCAPS-1D, a novel n-i-p device architecture ($FTO/SnO_2/Cs_2PtI_6/MoO_3/C$) is theoretically investigated in this work. Theoretical investigations were conducted to optimize the performance structure of the device by varying the thickness of the perovskite and selective charge transport layer, the absorber and interface defect density, the operating temperature, the back contact, the series and shunt resistance, respectively. At 300 K, the improved device demonstrated an outstanding PCE of 23.52%, which is greater than the previously reported figures. These findings will provide theoretical recommendations for boosting the performance of Cs_2PtI_6-based PSCs and pave the way for the broad adoption of environmentally friendly and stable perovskites.

2 Theoretical simulation

For our numerical simulations, we used SCAPS-1D software version 3.3.10. In SCAPS-1D a total of seven layers, along with different front and back contacts, could be employed as input. One can analyze J–V characteristics, ac characteristics (C–f and C–V), device efficiency (η), open circuit voltage (V_{oc}), fill factor (FF), short circuit current density (J_{sc}), spectral response (QE) of device using SCAPS-1D. The simulations are based on three

equations: Poisson's eqn (1) and continuity equation for holes and electrons eqn (2):

$$\frac{d^2\psi}{dx^2} = \frac{e}{\varepsilon_o \varepsilon_r}\left[p(x) - n(x) + N_D - N_A + \rho_p - \rho_n\right] \quad (1)$$

where ψ is electrostatic potential, n and p are electron and hole concentrations, ε_o is vacuum and ε_r is relative permittivity, N_D and N_A are donor and acceptor doping density, ρ_n, ρ_p are electrons and holes distribution,

$$\frac{dJ_p}{dx} = \frac{dJ_n}{dx} = G - R \quad (2)$$

where G is generation rate and R is recombination rate, J_p and J_n are holes and electron current densities.

Carrier transport occurs according to drift and diffusion equations:

$$J_n = \mu_n n \frac{d\varphi}{dx} + D_n \frac{dn}{dx} \quad (3)$$

$$J_p = \mu_p p \frac{d\varphi}{dx} + D_p \frac{dp}{dx} \quad (4)$$

In order to achieve a higher level of efficiency, the hole transport layer (HTL) and electron transport layer (ETL) must have band gap edges that correspond with the VBM and CBM of the active layers. Fig. 1 and 2 illustrate the band gap alignment of MoO_3, SnO_2, and Cs_2PtI_6, as well as the back and front device contacts. The lowest unoccupied molecular orbital (LUMO) of SnO_2 (ETL) is in excellent alignment with the conduction band of Cs_2PtI_6. Likewise, the highest occupied molecular orbital (HOMO) of MoO_3 (HTL) is well-aligned with the valence band level of an absorbing material.

Table 1 displays the input parameters for FTO, SnO_2, Cs_2PtI_6, and MoO_3 derived from the literature. The work functions of front contact (FTO) and back contact (carbon) are 4.4 eV and 5.0 eV, respectively. Thermal velocity of both holes and electrons is 1×10^7 (at 300 K). For all defects, defect type is taken as
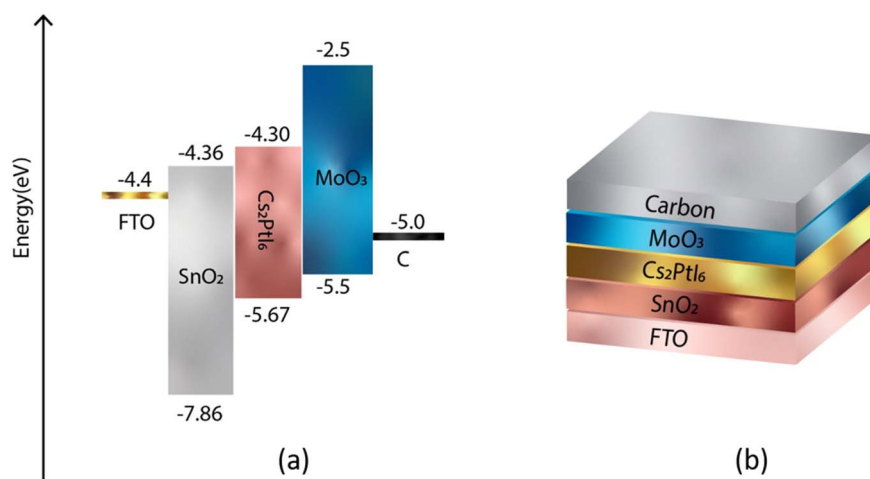

Fig. 1 (a) Energy level diagram of FTO, ETL (SnO_2), perovskite (Cs_2PtI_6), HTL (MoO_3), back contact C (b) a schematic of device structure of n-i-p $FTO/SnO_2/Cs_2PtI_6/MoO_3/C$ under AM 1.5 spectra, constant illumination 1000 W m^{-2}, working temperature 300 K, shunt resistance 4200 Ω cm^2 and series resistance 1 Ω cm^2.

Fig. 2 (a) Energy level diagram of FTO, ETL (SnO_2), perovskite (Cs_2PtI_6), HTL (MoO_3), back contact GO (b) a schematic of device structure of n-i-p FTO/SnO_2/Cs_2PtI_6/MoO_3/GO under AM 1.5 spectra, constant illumination 1000 W m^{-2}, working temperature 300 K, shunt resistance 4200 Ω cm^2 and series resistance 1 Ω cm^2.
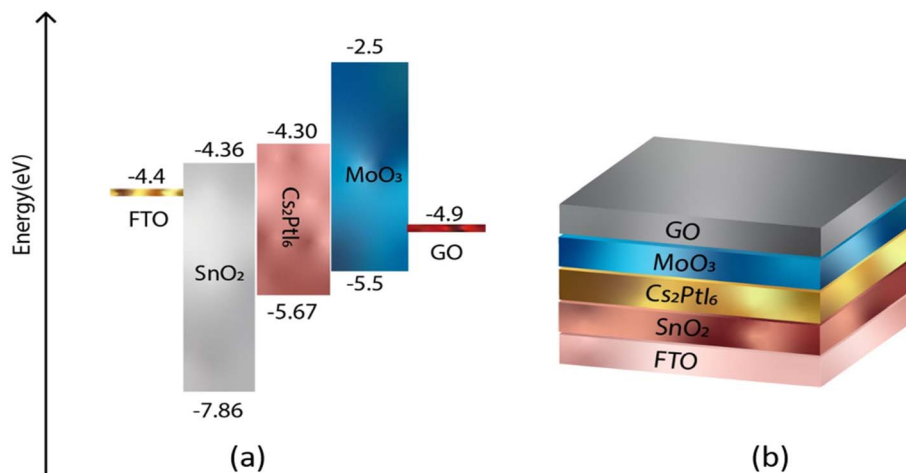
Table 1 Input parameters for materials used in the device architecture FTO/SnO_2/Cs_2PtI_6/MoO_3/C

Input parameters	FTO	n-SnO_2	Cs_2PtI_6	n-MoO_3
Thickness, d (nm)	500	10	300	30
Band gap, E_g (eV)	3.5	3.5	1.37	3
Electron affinity, χ	4	4	4.3	2.5
Permittivity, ε_r	9	9	4.8	12.5
Electron mobility, μ_n (cm^2 V^{-1} s^{-1})	20	20	62.6	25
Hole mobility, μ_p (cm^2 V^{-1} s^{-1})	10	10	62.6	100
Effective density of states at CB, N_c (cm^{-3})	2.2×10^{18}	2.2×10^{17}	3.0×10^{14}	2.2×10^{18}
Effective density of states at VB, N_v (cm^{-3})	1.8×10^{19}	2.2×10^{16}	1.0×10^{17}	1.8×10^{19}
Density of n-type doping, N_D (cm^{-3})	1×10^{19}	1×10^{18}	1×10^{12}	0
Density of p-type doping, N_A (cm^{-3})	0	0	1×10^{15}	1×10^{-18}
Defect density, N_t (cm^{-3})	—	1×10^{15}	1×10^{17}	1×10^{15}
Capture cross-section electron (cm^2)	—	2×10^{-14}	1×10^{-15}	1×10^{-15}
Capture cross-section holes (cm^2)	—	2×10^{-14}	1×10^{-15}	1×10^{-15}
Reference	24	25	23 and 26	27

neutral, characteristic energy is 1.0 eV, energetic distribution is single. Defect density for both interfaces is 1×10^{13}, capture cross-section of electrons and holes is 1×10^{18}. All simulations were performed under AM 1.5 spectra, constant illumination 1000 W m^{-2}, working temperature 300 K, shunt resistance 4200 Ω cm^2 and series resistance 1 Ω cm^2.

3 Result and discussion

3.1 Effect of HTL thickness

To ensure that the same number of charge carriers reach terminals instantaneously with a low recombination probability, the thickness of the HTL is generally higher than that of the electron transport layer. In general, the recombination rate increases as the HTL's thickness decreases. Fig. 3 illustrates the impact of HTL thickness on device properties. Here, MoO_3 thickness ranged from 20 to 100 nm. Both V_{oc} and J_{sc} increased with increasing MoO_3 thickness (Table S1†), reaching saturation at 32 nm with a maximum of 26.163 mA cm^{-2} and 1.14 V,

respectively. Both PCE and FF increased with increasing thickness until reaching a maximum value, after which they reduced till reaching a constant value.

When the HTL thickness is too thin, current leakage and low shunt resistance can occur, resulting in a lower FF.[28] In our case, it decreased after reaching the highest FF value of 80.44% at 22 nm. It could be because increasing HTL thickness increased series resistance, causing the FF to drop to 75.74% at 60 nm before remaining unchanged.[28] At 24 nm, the maximum efficiency of 23.13%, V_{oc} of 1.118 V, J_{sc} of 26.158 mA cm^{-2}, and FF of 79.105% was obtained. Thus, the optimum HTL thickness of 24 nm was utilized for our subsequent devices.

3.2 Effect of absorbing layer thickness

In designing a solar cell, the thickness of the perovskite is crucial because it directly affects the device parameters. Because electron–hole pair generation occurs in the absorbing layer, increasing thickness increases incident light absorption and generates more electron–hole pairs. This increases the device's
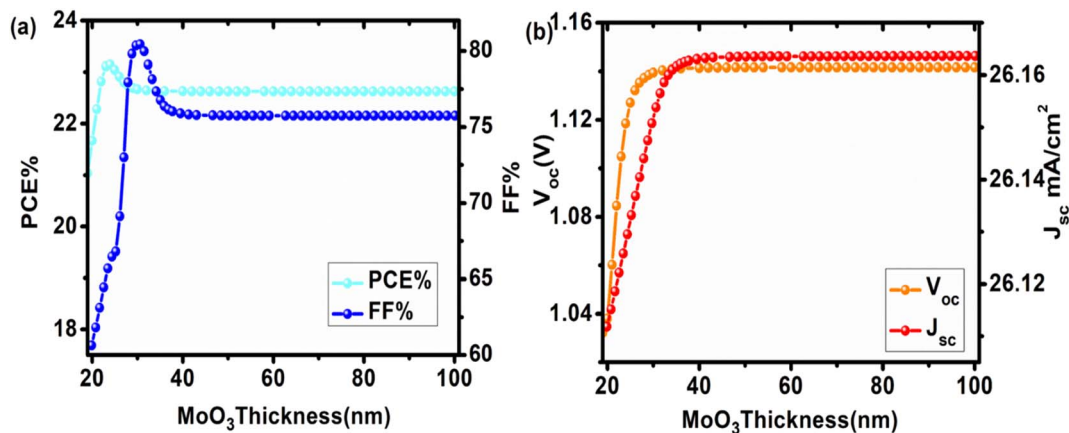
Fig. 3 Influence of varying MoO_3 (HTL) thickness (20–100 nm) on device performance of configuration $FTO/SnO_2/Cs_2PtI_6/MoO_3/C$ PSC (a) comparison of PCE and FF, (b) comparison of V_{oc} and J_{sc}.

PCE, but only up to a certain point, after which efficiency degrades. In this case, the perovskite thickness should not exceed the carrier diffusion length; otherwise, recombination and back contact recombination density would increase. The influence of absorbing layer thickness on PCE, J_{sc}, V_{oc}, and FF is shown in Fig. 4 and Table S2†. Here, the Cs_2PtI_6 thickness was varied from 100 nm to 1000 nm. J_{sc} increased as perovskite

thickness increased. Because Cs_2PtI_6 has a higher absorption coefficient (4×10^5 cm^{-1}),[22] increasing thickness allows more light to be absorbed, resulting in more electron–hole pair generation. Although the length of charge carrier diffusion in these perovskites is also longer, these electron–hole pairs can reach the corresponding electrodes to generate power.[29] The J_{sc} at 680 nm reached a maximum of 30.37 mA cm^{-2} before
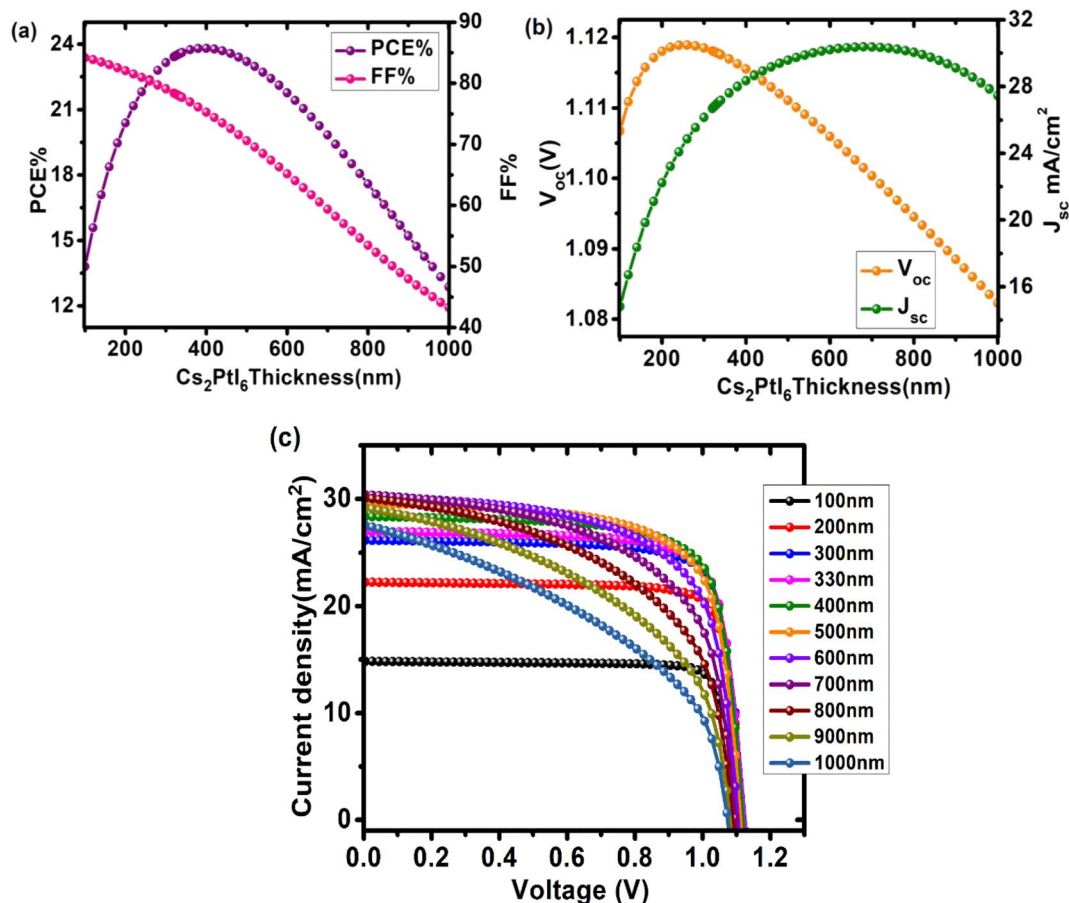

Fig. 4 Impact of changing Cs_2PtI_6 (absorber layer) thickness (100–1000 nm) on performance of cell configuration $FTO/SnO_2/Cs_2PtI_6/MoO_3/C$ PSC (a) PCE and FF, (b) V_{oc} and J_{sc}, (c) comparison of J–V curves at different Cs_2PtI_6 thicknesses.
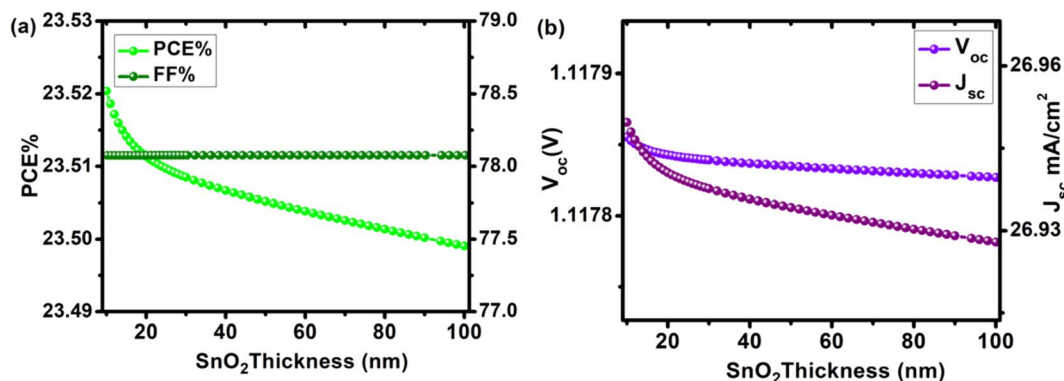
Fig. 5 Device performance of configuration FTO/SnO$_2$/Cs$_2$PtI$_6$/MoO$_3$/C PSC as a function of increasing SnO$_2$ (ETL) thickness (10–100 nm) (a) PCE and FF, (b) V_{oc} and J_{sc}.

decreasing. These findings are consistent with previously reported data.[30]

PCE also increased as the thickness increased, but only up to 400 nm, where the maximum efficiency of 23.8% is observed, and then it decreased. As a result of a higher absorption coefficient, a higher number of charge carriers are generated, resulting in the maximum possible increase in efficiency.

Following this optimal thickness, PCE decreased. Despite the higher level of electron and hole generation, the perovskite thickness exceeds the carrier diffusion length of electrons and holes, resulting in increased recombination rates and decreased efficiency. When thickness increases, so do pinholes, cracks, and traps, resulting in a decline in PCE.[29]
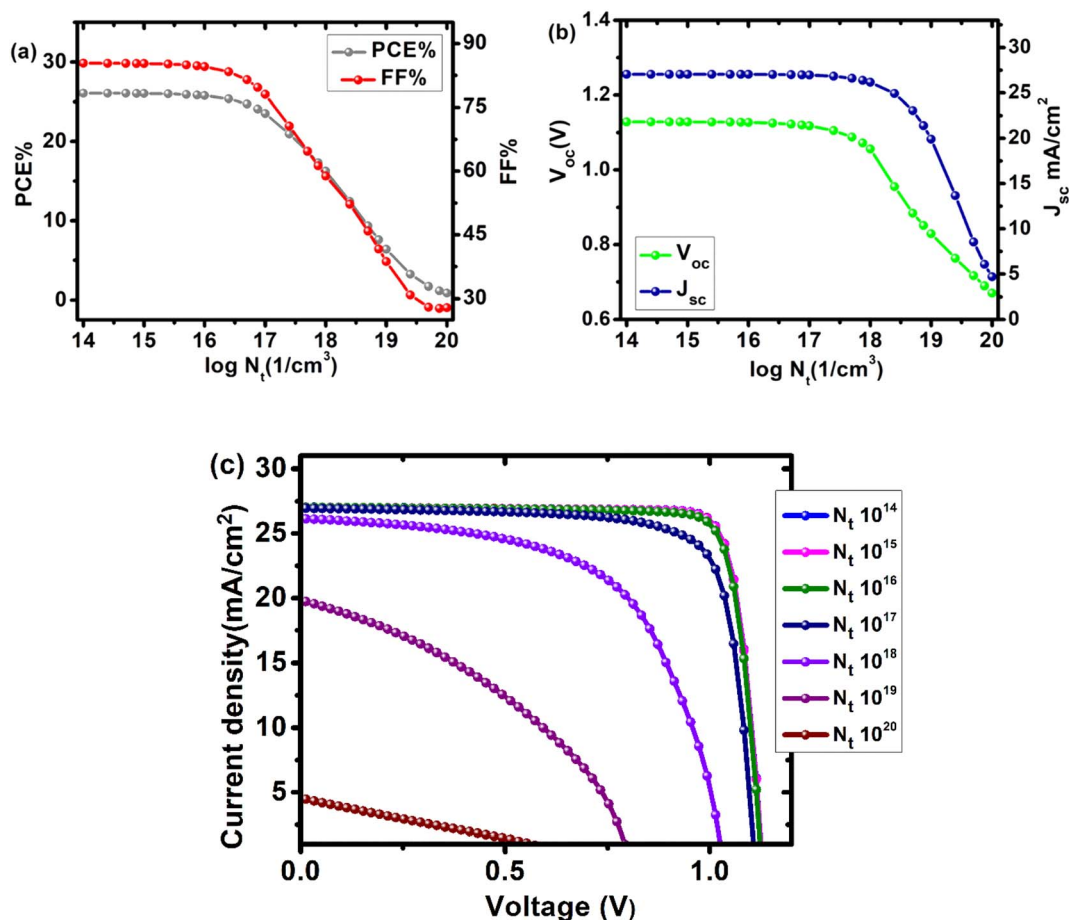

Fig. 6 Effect of Cs$_2$PtI$_6$ (absorber layer) defect density (10^{14}–10^{20} cm^{-3}) on device parameters of cell configuration FTO/SnO$_2$/Cs$_2$PtI$_6$/MoO$_3$/C (a) PCE and FF, (b) V_{oc} and J_{sc}, (c) a comparison of J–V curves of device at different absorber layer defect densities.

Table 2 Solar cell parameters at various Cs_2PtI_6 (perovskite absorber layer) defect densities (N_t) for configuration FTO/SnO$_2$/Cs$_2$PtI$_6$/MoO$_3$/C

Defect density(cm^{-3})	V_{oc} (V)	J_{sc} (mA cm^{-2})	FF (%)	PCE (%)
1×10^{14}	1.1287	27.0396	85.37	26.05
1×10^{15}	1.1286	27.0788	85.29	26.03
1×10^{16}	1.1275	27.0307	84.55	25.77
1×10^{17}	1.1178	26.9497	78.08	23.52
1×10^{18}	1.0560	26.1602	58.83	16.25
1×10^{19}	0.8291	19.9050	38.68	6.38
1×10^{20}	0.6708	4.6933	27.87	0.88

V_{oc} increased with perovskite thickness until it reached a maximum of 1.11 V at 260 nm, after which it dropped precipitously. V_{oc} is defined as:
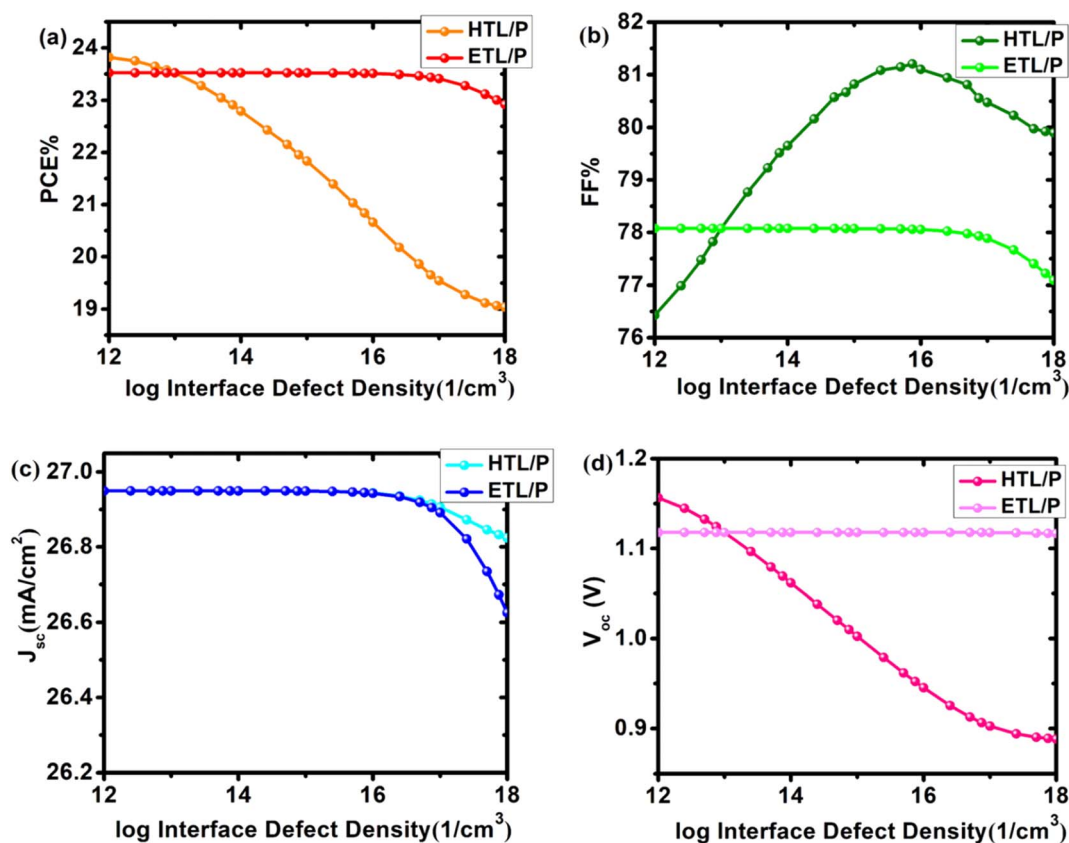
$$V_{OC} = \frac{nkT}{q} \ln\left(\frac{I_L}{I_O} + 1\right)$$

where n is an ideality factor, q is the electrical charge, T is temperature, k is the Boltzmann constant, I_o is the dark saturation current, and I_L is light generated current. V_{oc} is affected by cracks, pinholes, and other layer defects and is dependent on surface morphology. The absorber layer is relatively thinner during the early increase in V_{oc}, resulting in a lower recombination rate. Furthermore, as the length of the diffusion carrier increases, so does the value of the dark saturation current. This slower recombination rate eventually leads to a higher concentration of carriers, which raises the light-generated current I_L. However, as the thickness of the absorbing layer continues to increase, the recombination rate, along with I_o, increases, causing the V_{oc} to fall abruptly and squarely.[29] The FF relates to charge route resistance and represents the efficiency with which holes and electrons transit the cell without loss.[31,32] As the perovskite's thickness increased, the fill factor decreased. FF decreased from 78.3% at 100 nm to 43.29% at 1000 nm as the thickness increased.

3.3 Effect of ETL thickness

The dependence of solar cell properties on ETL (SnO$_2$) was studied by varying the thickness of the electron transport layer from 10 nm to 100 nm (Table S3 †). To prevent incident photons from being absorbed and producing electron–hole pairs in the electron transport layer, it is common to practice keeping the n-type layer (ETL) thinner than the equivalent p-type layer (HTL). ETL is also kept thinner to allow incident photons to pass through to the absorber and HTLs beneath it. The influence of ETL thickness change on cell metrics is depicted in Fig. 5. By increasing ETL thickness, no improvement in cell metrics was observed. PCE, V_{oc}, J_{sc}, and FF were 23.52%, 1.11782 V, 26.95 mA

Fig. 7 Solar cell output as a function of varying defect density N_t (10^{12}–10^{18} cm^{-3}) of interfaces MoO$_3$/Cs$_2$PtI$_6$ (HTL/P) and SnO$_2$/Cs$_2$PtI$_6$ (ETL/P) of device configuration FTO/SnO$_2$/Cs$_2$PtI$_6$/MoO$_3$/C (a) efficiency (PCE), (b) fill factor (FF), (c) short circuit current J_{sc} and (d) open circuit voltage V_{oc}.

cm^{-2}, and 78.076% at 10 nm, and 23.49%, 1.11780 V, 26.93 mA cm^{-2}, and 78.078% at 100 nm, respectively. With the increase in ETL thickness, the change in V_{oc} was insignificant (from 1.11782 V to 1.11780 V, a loss of just 0.0017%), indicating that by varying the thickness of SnO$_2$ ETL, charge carrier leakage at the interface is limited. When the thickness of a device grows, fewer electron–hole pairs are formed, and charge carrier recombination occurs, resulting in a drop in overall device efficiency. Our optimal device has an ETL thickness of 10 nm, with PCE of 23.52%, J_{sc} of 26.95 mA cm^{-2}, V_{oc} of 1.1178 V, and FF of 8.076%.

3.4 Perovskite (absorber) layer defect density

The optoelectronic properties of an absorbent layer are highly dependent on its preparation method, thickness, and analysis methodologies. Furthermore, defects in the system could change the optoelectronic properties. Defects were introduced into the absorbent layer to make our device appear more realistic. The defect density ranged from 10^{14}–10^{20} cm^{-3}. Fig. 6 depicts the effect of Cs$_2$PtI$_6$ defect density on cell parameters. The recombination rate increases and all cell characteristics decrease as the number of cracks and pinholes increases due to an increase in N_t. An efficiency of 26% was observed with a defect density of 1×10^{15} cm^{-3}. We chose a defect density of 1×10^{17} cm^{-3} for our device, which yielded an efficiency of 23.5% (Table 2). Material defects must be reduced in order for the device to be effective, and it must be smooth and free of cracks.

3.5 Effect of interface defect density

Due to a mismatch in the crystallographic structures of the ETL, HTL, and absorbing layer, interfaces with a plethora of dislocations could form, hence reducing junction quality and triggering recombination. The defect density was varied between 10^{12} cm^{-3} and 10^{18} cm^{-3} to explore the global impact of interface defect density on cell performance. Fig. 7 depicts the impact of interface defect density on cell characteristics. There

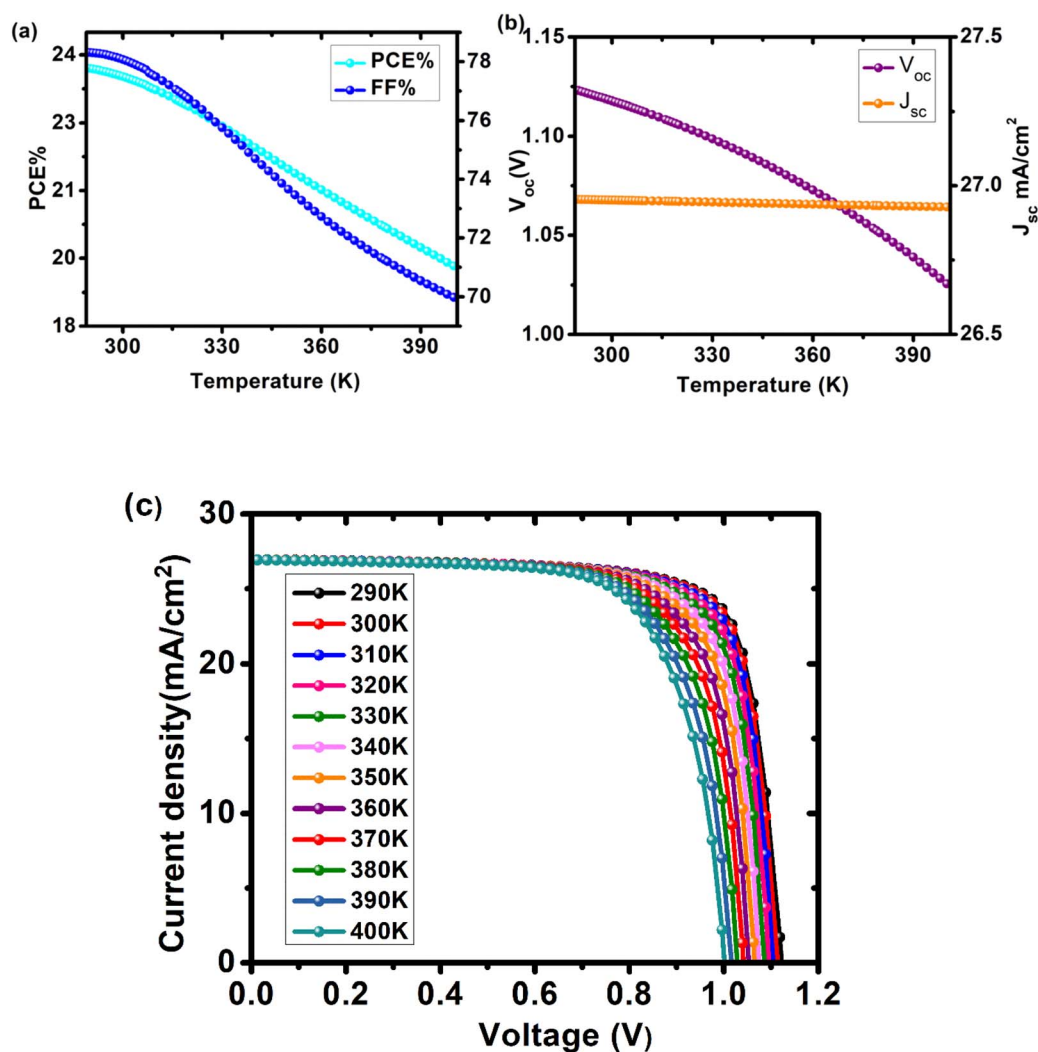**Fig. 8** Influence of changing operating temperature (290–400 K) on parameters of cell configuration FTO/SnO$_2$/Cs$_2$PtI$_6$/MoO$_3$/C (a) PCE and FF, (b) V_{oc} and J_{sc}, (c) a comparison of J–V curves of device at different temperatures.

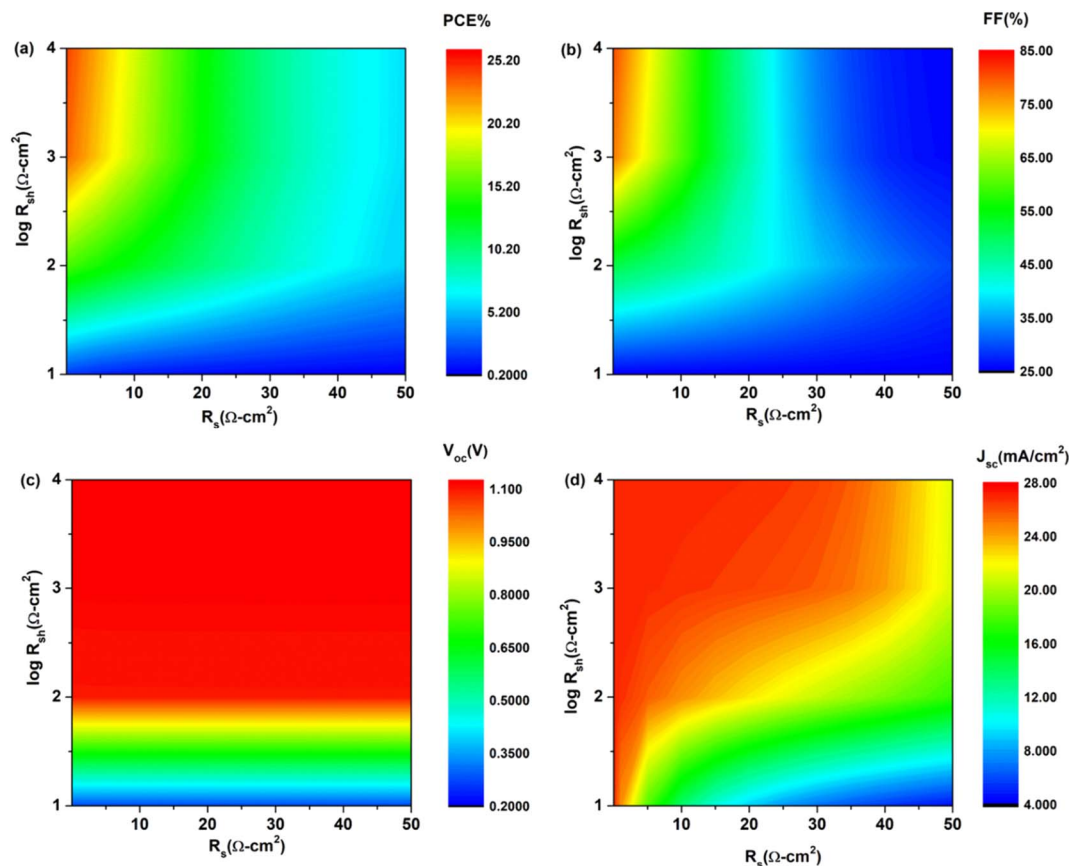**Fig. 9** Device parameters as function of increases resistance R_s (0.01 to 50 Ω cm^2) of cell configuration FTO/SnO$_2$/Cs$_2$PtI$_6$/MoO$_3$/C (a) PCE, (b) FF, (c) V_{oc} and (d) J_{sc}.

was no significant change in PCE and V_{oc} when the defect density of the ETL/perovskite layer (SnO$_2$/Cs$_2$PtI$_6$) was varied (Table S4 †). However, with the increase in the interface defect density of the HTL/perovskite layer (MoO$_3$/Cs$_2$PtI$_6$), the efficiency and V_{oc} drastically degraded (Table S5 †). The cell's PCE decreased from 23.8% at 10^{12} N_t to 19.04% at 10^{18} N_t. V_{oc} tumbled by 23%, from 1.156 V to 0.888 V.

As N_t increases, there is no discernible change in J_{sc}. It only decreases when the prevalence of interface defects increases. By increasing the N_t of the HTL/P layer to 10^{18} cm^{-3} (from 26.94 mA cm^{-2} to 26.62 mA cm^{-2}), J_{sc} decreased by 1.19%. Both interfaces have an effect on the fill factor. The fill factor decreased from 78.08% to 77.08% when ETL/perovskite defects

increased. In the case of the HTL/perovskite layer, the defect density increased from 76.42% to an all-time high of 81.2% at N_t 10^{15} cm^{-3}, before decreasing to 79.90% at defect density 10^{18} cm^{-3}. We have selected a defect density of 10^{13} cm^{-3} for both device interfaces.

3.6 Effect of temperature

Temperature has a direct effect on hole mobility, electron mobility, and carrier concentration, all of which affect cell performance.[33] The device's performance was investigated at temperatures ranging from 290 K to 400 K. Eqn (5) shows the effect of temperature on V_{oc}:[34]

Table 3 Solar cell parameters at different values of series resistance R_S (Ω cm^2) for configuration FTO/SnO$_2$/Cs$_2$PtI$_6$/MoO$_3$/C

Series resistance (R_s) (Ω cm^2)	V_{oc} (V)	J_{sc} (mA cm^{-2})	FF (%)	PCE (%)
0.01	1.11770	26.959	79.99	24.10
0.1	1.11771	26.958	79.81	24.05
1	1.11782	26.949	78.07	23.52
5	1.11805	26.908	70.45	21.19
10	1.11815	26.847	61.26	18.39
25	1.11820	26.501	38.02	11.27
40	1.11827	24.528	27.12	7.44
50	1.11830	21.068	25.57	6.03

Fig. 10 Quantum efficiency of device configuration FTO/SnO$_2$/Cs$_2$PtI$_6$/MoO$_3$/C at different Cs$_2$PtI$_6$ thicknesses (100–1000 nm).

Table 4 Solar cell parameters at different values of back contact work function (eV) for configuration FTO/SnO$_2$/Cs$_2$PtI$_6$/MoO$_3$/C

Back contact	Work function (Φ)	V_{oc} (V)	J_{sc} (mA cm^{-2})	FF (%)	PCE (%)
Cu[36]	4.53	0.72	26.822	67.60	13.14
Ni[37]	4.61	0.80	26.861	69.85	15.04
Ag[38]	4.74	0.92	26.905	73.11	18.14
Fe[39]	4.81	0.98	26.921	74.94	19.80
GO[40]	4.9	1.05	26.937	76.98	21.94
C[41]	5.0	1.12	26.949	78.08	23.52

$$V_{oc} = \frac{nKT}{q} \log\left(\frac{J_{sc}}{J_o} + 1\right) \qquad (5)$$

where V_{oc} is open circuit voltage, K is Boltzmann constant, q is the electronic charge, n is ideality constant, T is temperature, J_o is reverse saturation current and J_{sc} is current density. It has been observed that with the increase in the operating temperature, reverse saturation current density increases, and V_{oc} decreases exponentially.[35] Fig. 8 and Table S6† depict the effect of temperature on device performance. All cell metrics degraded with each increase in temperature. V_{oc} decreased from 1.12295 V at 290 K to 1.02557 V at 400 K. The FF decreased from 78.31% to 69.98%. There was no discernible change in the device's current density. It decreased by 0.09% from 26.9536 to 26.9282 mA cm^{-2}. The device's PCE fell from 23.7% to 19.0%. As the temperature rises, the phonons are triggered, increasing charge carrier scattering, this modifies the material's conductivity. As a result, overall performance declined. For our device, we have chosen an optimal working temperature of 300 K where PCE is 23.52%, V_{oc} is 1.11782 V, J_{sc} is 26.9519 mA cm^{-2} and FF is 78.07%.

3.7 Effect of resistance on device parameters

Device performance is immensely influenced by both series and shunt resistance. Series resistance is due to interfaces, back and front contact, and resistance to flow of current while R_{sh} is the

aftereffect of reverse saturation current. Both high R_{sh} and low R_s are likely to deliver better device performance. The effect of R_s and R_{sh} on device parameters was studied by altering values between 0.01–50 Ω cm^2 and 10–10000 Ω cm^2. Eqn (6) can be used to understand the effect of resistance on device performance:[34]

$$I_{sc} = I_L + I_O\left(e^{\frac{V_{oc}q}{nKT}} - 1\right) - \frac{V_{oc} + I_{sc}R_s}{R_{sh}} \qquad (6)$$

where I_{sc} is short circuit current, R_{sh} is shunt resistance, R_s is series resistance, I_L is light induced current, and I_O is reverse saturation current.

According to the above equation, when series resistance increases, short circuit current will decrease. This would have a direct effect on the device's efficiency and FF. The impact of series and shunt resistance on device parameters is seen in Fig. 9. PCE and FF drop as R_s increases, but J_{sc} is only affected at higher R_s levels and V_{oc} is unaffected. At R_s 0.01 Ω cm^2, a PCE high of 24.1% is measured. PCE dropped to 6.03% as the value of R_s increased from 0.01 to 50 Ω cm^2. Similar to PCE, the fill factor decreased from 79.9% to 25.57% (Table 3). The initial increase in resistance had little effect on the J_{sc}, but at 50 Ω cm^2, it decreased from 26.959 mA cm^{-2} to 21.068 mA cm^{-2}. In case of R_{sh}, both PCE and FF increased with an increase in R_{sh} but only at low R_s, V_{oc} isn't much affected by R_{sh} while J_{sc} increased with increase in R_{sh}. These findings are consistent with those of other researchers. Hence, for improved device performance, the series resistance should be kept low while shunt resistance should be kept high.

3.8 Quantum efficiency studies

Quantum efficiency (QE) is the probability that an incident photon will transfer an electron to the device's external circuit. Yet, this property is independent of the incident spectrum. Fig. 10 demonstrates the effect of absorbing layer thickness on quantum efficiency for wavelengths between 300 and 900 nm. QE increased with increasing perovskite thickness up to a maximum of 98.9% before declining. At 100 nm, the QE was 70%. At 400 nm, the concentration increased from 91.6% at 200 nm to 98.85%. A further increase in thickness did not result in a significant increase in QE, as QE at 500 nm was already 98.9%. QE decreased to 86.1% at 1000 nm as thickness rose further. In the range of 354–550 nm, high quantum efficiency was observed. As its thickness increased, its wavelength range changed towards longer values. Maximum QE was observed at the same wavelength (354.5 nm) for perovskite thicknesses between 100 nm and 600 nm, however as thickness increased, this wavelength shifted to longer wavelengths. The high QE of perovskite is due to its high absorption coefficient (4 × 10^5 cm^{-1}).[22] This study demonstrates that Cs$_2$PtI$_6$ is optically active and may have additional applications in photovoltaics.

3.9 Effect of back contact on device parameters

The back contact of solar cells is essential to their performance because it absorbs electrons from the absorbing layer. For
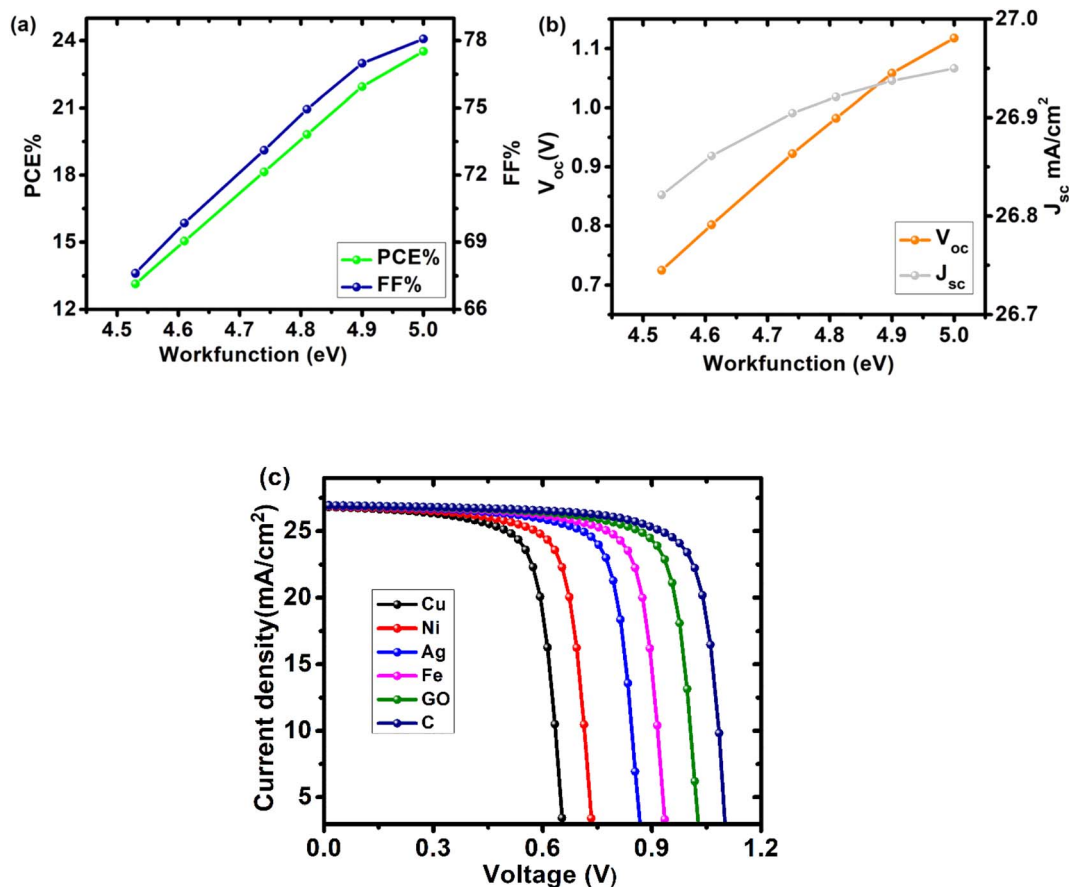
Fig. 11 Device performance as a function of back contact work function for cell configuration $FTO/SnO_2/Cs_2PtI_6/MoO_3/C$ (a) PCE and FF, (b) V_{oc} and J_{sc}, (c) $J-V$ curve of device with different back contacts.
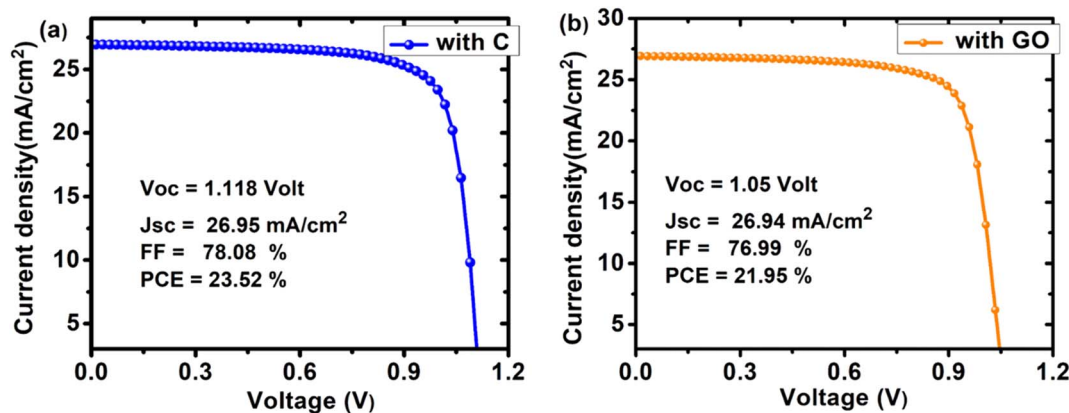

Fig. 12 $J-V$ curves of the optimized device having configuration (a) $FTO/SnO_2/Cs_2PtI_6/MoO_3/C$ and (b) $FTO/SnO_2/Cs_2PtI_6/MoO_3/GO$.

ohmic contact with the HTL or the absorber layer, a high work function is necessary. Fig. 9 illustrates the effect of the back contact work function on the device's properties. Cu, Ni, Ag, Fe, GO, and C were used as back contact materials in our device. As work function increased, efficiency grew, beginning at 13.14% with Cu as the back contact and reaching a high of 23.52% with carbon as the back contact. The other cell metrics likewise

improved when the back contact's work function increased. As the work function of the back contact increases, the barrier height for charge carriers at the back contact decreases, leading to an overall improvement in cell characteristics. Table 4 compares cell properties to the work function of the back contact (Fig. 11 and 12).

Table 5 Performance comparison of our work and preceding work on Cs_2PtI_6 based PSCs

Device architecture	V_{oc} (V)	J_{sc} (mA cm^{-2})	FF (%)	PCE (%)	Experimental/simulation	Reference
ITO/SnO$_2$/Cs$_2$PtI$_6$/spiro-OMeTAD/Au	0.73	1.20	82.00	0.72	Experimental	23
FTO/CdS/Cs$_2$PtI$_6$ with EDA/carbon/Cu	1.07	19.84	65.03	13.88	Experimental	22
FTO/CdS/Cs$_2$PtI$_6$/carbon/Cu	1.20	20.20	41.51	10.06	Experimental	22
FTO/ZnO/Cs$_2$PtI$_6$/MoO$_3$/Cu	1.3856	16.1070	75.54	16.85	Simulation	26
FTO/ZnO/Cs$_2$PtI$_6$/MoO$_3$/C	1.4105	16.1122	90.01	20.45	Simulation	26
FTO/CdS/Cs$_2$PtI$_6$/MoO$_3$/Cu	1.11	20.14	61	13.9	Simulation	30
FTO/CdS/Cs$_2$PtI$_6$/Cu$_2$O/Cu	1.1	20.4	62	14.2	Simulation	30
FTO/CdS/Cs$_2$PtI$_6$/CuI/Cu	1.12	20.13	60	13.7	Simulation	30
FTO/ICZSO/ Cs$_2$PtI$_6$/Cu$_2$O/C	1.13	22.2	59.2	14.8	Simulation	30
FTO/ZnSe/Cs$_2$PtI$_6$/Cu$_2$O/C	1.12	22.3	58	14.7	Simulation	30
FTO/WS$_2$/Cs$_2$PtI$_6$/Cu$_2$O/C	1.1	28.1	52.4	16.3	Simulation	30
FTO/SnO$_2$/Cs$_2$PtI$_6$/MoO$_3$/GO	**1.05**	**26.94**	**76.99**	**21.95**	**Simulation**	**This work**
FTO/SnO$_2$/Cs$_2$PtI$_6$/MoO$_3$/C	**1.118**	**26.95**	**78.08**	**23.52**	**Simulation**	**This work**

4 Conclusion

We have reported the design optimization of an ecologically friendly, lead-free planar Cs_2PtI_6 solar cell using MoO_3 as the HTL and SnO_2 as the ETL (Table 5). Our research demonstrates that MoO_3 (HTL), Cs_2PtI_6, and SnO_2 have a considerable effect on device performance. The impact of varying the defect densities of the interface and absorber layers demonstrated that these parameters are crucial for device performance and that fewer defects are necessary for improved device performance. It was determined that series resistance had little influence on V_{oc} but a substantial effect on PCE, FF, and J_{sc}. Effect of shunt resistance showed that both PCE and FF increase with an increase in R_{sh} (at low R_s), V_{oc} isn't much affected by R_{sh} while J_{sc} increases with an increase in R_{sh}. In addition, the effect of temperature on the device's functionality revealed that lower temperatures led to improved performance. The material's spectral response revealed that it was active. Cu, Ni, Ag, Fe, Go, and C were employed as back contacts, with C's work function of 5.0 eV being the best. The optimal device was the n-i-p device with the structure FTO/SnO$_2$/Cs$_2$PtI$_6$/MoO$_3$/C with a PCE of 23.52% (V_{oc} of 1.118 V, J_{sc} of 26.95 mA cm^{-2}, FF of 78.08%).

Conflicts of interest

There are no conflicts to declare.

References

1 H. Y. F. Chen, W. T. Tang, J. J. He, M. S. Yin, Y. B. Wang, F. X. Xie, E. B. Bi, X. D. Yang, M. Gratzel and L. Y. Han, *Nature*, 2017, **550**, 92–95, DOI: **10.1038/nature23877**.

2 Z. Wang, *et al.*, Efficient ambient-air-stable solar cells with 2D–3D heterostructured butylammonium-caesium-formamidinium lead halide perovskites, *Nat. Energy*, 2017, **2**(9), 1–10, DOI: **10.1038/nenergy.2017.135**.

3 G. E. Eperon, *et al.*, Formamidinium lead trihalide: a broadly tunable perovskite for efficient planar heterojunction solar cells, *Energy Environ. Sci.*, 2014, **7**(3), 982–988, DOI: **10.1039/C3EE43822H**.

4 Z. Shi, *et al.*, Strategy of solution-processed all-inorganic heterostructure for humidity/temperature-stable perovskite quantum dot light-emitting diodes, *ACS Nano*, 2018, **12**(2), 1462–1472, DOI: **10.1021/acsnano.7b07856**.

5 M. Jeong, *et al.*, Large-area perovskite solar cells employing spiro-Naph hole transport material, *Nat. Photonics*, 2022, **16**(2), 119–125, DOI: **10.1038/s41566-021-00931-7**.

6 R. Lin, *et al.*, All-perovskite tandem solar cells with improved grain surface passivation, *Nature*, 2022, **603**(7899), 73–78. **https://www.nature.com/articles/s41586-021-04372-8**.

7 K. Xiao, *et al.*, All-perovskite tandem solar cells with 24.2% certified efficiency and area over 1 cm2 using surface-anchoring zwitterionic antioxidant, *Nat. Energy*, 2020, **5**(11), 870–880, DOI: **10.1038/s41560-020-00705-5**.

8 S. D. Stranks and H. J. Snaith, Metal-halide perovskites for photovoltaic and light-emitting devices, *Nat. Nanotechnol.*, 2015, **10**(5), 391–402, DOI: **10.1038/nnano.2015.90**.

9 M. T. Hörantner and H. J. Snaith, Predicting and optimizing the energy yield of perovskite-on-silicon tandem solar cells under real world conditions, *Energy Environ. Sci.*, 2017, **10**(9), 1983–1993, DOI: **10.1039/C7EE01232B**.

10 T. A. Berhe, *et al.*, Organometal halide perovskite solar cells: degradation and stability, *Energy Environ. Sci.*, 2016, **9**(2), 323–356, DOI: **10.1039/C5EE02733K**.

11 E. Jokar, *et al.*, Robust tin-based perovskite solar cells with hybrid organic cations to attain efficiency approaching 10%, *Adv. Mater.*, 2019, **31**(2), 1804835, DOI: **10.1002/adma.201804835**.

12 M. Chen, *et al.*, Cesium titanium (IV) bromide thin films based stable lead-free perovskite solar cells, *Joule*, 2018, **2**(3), 558–570, DOI: **10.1016/j.joule.2018.01.009**.

13 S. Weber, *et al.*, Influence of the iodide to bromide ratio on crystallographic and optoelectronic properties of rubidium antimony halide perovskites, *ACS Appl. Energy Mater.*, 2018, **2**(1), 539–547, DOI: **10.1021/acsaem.8b01572**.

14 Y. Hu, *et al.*, Enhancing moisture-tolerance and photovoltaic performances of FAPbI$_3$ by bismuth incorporation, *J. Mater. Chem. A*, 2017, **5**(48), 25258–25265, DOI: **10.1039/C7TA08824H**.

15 F. Umar, *et al.*, Dimensionality controlling of Cs$_3$Sb$_2$I$_9$ for efficient all-inorganic planar thin film solar cells by

HCl-assisted solution method, *Adv. Opt. Mater.*, 2019, **7**(5), 1801368, DOI: **10.1002/adom.201801368**.

16 W. Dai, *et al.*, Lead-free, stable, and effective double FA$_4$Ge$_{II}$Sb$_{III}$Cl1$_2$ perovskite for photovoltaic applications, *Sol. Energy Mater. Sol. Cells*, 2019, **192**, 140–146, DOI: **10.1016/j.solmat.2018.12.031**.

17 B. W. Park, *et al.*, Bismuth based hybrid perovskites A$_3$Bi$_2$I$_9$ (A: methylammonium or cesium) for solar cell application, *Adv. Mater.*, 2015, **27**(43), 6806–6813, DOI: **10.1002/adma.201501978**.

18 A. Kulkarni, *et al.*, Performance enhancement of AgBi$_2$I$_7$ solar cells by modulating a solvent-mediated adduct and tuning remnant BiI$_3$ in one-step crystallization, *Chem. Commun.*, 2019, **55**(28), 4031–4034, DOI: **10.1039/C9CC00733D**.

19 E. Greul, *et al.*, Highly stable, phase pure Cs$_2$AgBiBr$_6$ double perovskite thin films for optoelectronic applications, *J. Mater. Chem. A*, 2017, **5**(37), 19972–19981, DOI: **10.1039/C7TA06816F**.

20 K. Ahmad, *et al.*, A (CH$_3$NH$_3$)$_3$Bi$_2$I$_9$ Perovskite Based on a Two-Step Deposition Method: Lead-Free, Highly Stable, and with Enhanced Photovoltaic Performance, *ChemElectroChem*, 2019, **6**(4), 1192–1198, DOI: **10.1002/celc.201801322**.

21 L. Debbichi, *et al.*, Mixed valence perovskite Cs$_2$Au$_2$I$_6$: a potential material for thin-film Pb-free photovoltaic cells with ultrahigh efficiency, *Adv. Mater.*, 2018, **30**(12), 1707001, DOI: **10.1002/adma.201707001**.

22 D. Schwartz, *et al.*, Air Stable, High-Efficiency, Pt-Based Halide Perovskite Solar Cells with Long Carrier Lifetimes, *Phys. Status Solidi – Rapid Res. Lett.*, 2020, **14**(8), 2000182, DOI: **10.1002/pssr.202000182**.

23 S. Yang, *et al.*, Novel lead-free material Cs$_2$PtI$_6$ with narrow bandgap and ultra-stability for its photovoltaic application, *ACS Appl. Mater. Interfaces*, 2020, **12**(40), 44700–44709, DOI: **10.1021/acsami.0c11429**.

24 E. Karimi and S. Ghorashi, Investigation of the influence of different hole-transporting materials on the performance of perovskite solar cells, *Optik*, 2017, **130**, 650–658, DOI: **10.1016/j.ijleo.2016.10.122**.

25 N. Lakhdar and A. Hima, Electron transport material effect on performance of perovskite solar cells based on CH$_3$NH$_3$GeI$_3$, *Opt. Mater.*, 2020, **99**, 109517, DOI: **10.1016/j.optmat.2019.109517**.

26 M. Shamna and K. Sudheer, Device modeling of Cs$_2$PtI$_6$-based perovskite solar cell with diverse transport materials and contact metal electrodes: a comprehensive simulation study using solar cell capacitance simulator, *J. Photonics Energy*, 2022, **12**(3), 032211, DOI: **10.1117/1.JPE.12.032211**.

27 W. Li, *et al.*, Numerical analysis of the back interface for high efficiency wide band gap chalcopyrite solar cells, *Sol. Energy*, 2019, **180**, 207–215, DOI: **10.1016/j.solener.2019.01.018**.

28 L. Lin, *et al.*, Numerical analysis of inverted-structure perovskite solar cell based on all-inorganic charge transport layers, *J. Photonics Energy*, 2019, **9**(2), 024501, DOI: **10.1117/1.JPE.9.024501**.

29 K. Tan, *et al.*, Controllable design of solid-state perovskite solar cells by SCAPS device simulation, *Solid-State Electron.*, 2016, **126**, 75–80, DOI: **10.1016/j.sse.2016.09.012**.

30 H. H. AbdElAziz, *et al.*, Evaluating the performance of Cs$_2$PtI$_{6-x}$Br$_x$ for photovoltaic and photocatalytic applications using first-principles study and SCAPS-1D simulation, *Heliyon*, 2022, **8**(10), e10808, DOI: **10.1016/j.heliyon.2022.e10808**.

31 S. Ahmed, *et al.*, Simulation studies of Sn-based perovskites with Cu back-contact for non-toxic and non-corrosive devices, *J. Mater. Res.*, 2019, **34**(16), 2789–2795, DOI: **10.1557/jmr.2019.204**.

32 A. Hagfeldt, *et al.*, Dye-sensitized solar cells, *Chem. Rev.*, 2010, **110**(11), 6595–6663, DOI: **10.1021/cr900356p**.

33 S. Hossain, *et al.*, A numerical study on the prospects of high efficiency ultra thin zn$_x$ cd$_{1-x}$ s/cdte solar cell, *Chalcogenide Lett.*, 2011, **8**(4), 263–272.

34 K. Chakraborty, M. G. Choudhury and S. Paul, Numerical study of Cs$_2$TiX$_6$ (X= Br$^-$, I$^-$, F$^-$ and Cl$^-$) based perovskite solar cell using SCAPS-1D device simulation, *Sol. Energy*, 2019, **194**, 886–892, DOI: **10.1016/j.solener.2019.11.005**.

35 A. Fahrenbruch and R. Bube, *Fundamentals of Solar Cells: Photovoltaic Solar Energy Conversion*, Elsevier, 2012.

36 C. D. Zangmeister, *et al.*, Energy-level alignment and work function shifts for thiol-bound monolayers of conjugated molecules self-assembled on Ag, Cu, Au, and Pt, *Chem. Phys. Lett.*, 2007, **442**(4–6), 390–393, DOI: **10.1016/j.cplett.2007.06.012**.

37 W. Sachtler and G. Dorgelo, The surface of copper-nickel alloy films: I. Work function and phase composition, *J. Catal.*, 1965, **4**(6), 654–664, DOI: **10.1016/0021-9517(65)90265-4**.

38 A. Dweydari and C. Mee, Work function measurements on (100) and (110) surfaces of silver, *Phys. Status Solidi A*, 1975, **27**(1), 223–230, DOI: **10.1002/pssa.2210270126**.

39 R. Wu and A. Freeman, Structural, electronic, and magnetic properties of an open surface: Fe (111), *Phys. Rev. B: Condens. Matter Mater. Phys.*, 1993, **47**(7), 3904, DOI: **10.1103/PhysRevB.47.3904**.

40 J. P. Jayaraman, *et al.*, BiVO$_4$/Cs$_2$PtI$_6$ Vacancy-Ordered Halide Perovskite Heterojunction for Panchromatic Light Harvesting and Enhanced Charge Separation in Photoelectrochemical Water Oxidation, *ACS Appl. Mater. Interfaces*, 2021, **13**(14), 16267–16278, DOI: **10.1021/acsami.0c22654**.

41 M. Hamdan and A. K. Chandiran, Cs$_2$PtI$_6$ halide perovskite is stable to air, moisture, and extreme pH: application to photoelectrochemical solar water oxidation, *Angew. Chem.*, 2020, **132**(37), 16167–16172, DOI: **10.1002/ange.202000175**.